Materials & Design 218 (2022) 110709

Contents lists available at ScienceDirect

Materials & Design

journal homepage: www.elsevier.com/locate/matdes

Hybrid machine-learning and finite-element design for flexible metamaterial wings

Igor Zhilyaev [a], Dmitry Krushinsky [b], Mostafa Ranjbar [c], Anastasiia O. Krushynska [d,*]

[a] Institute of Polymer Engineering, University of Applied Sciences Northwestern Switzerland FHNW, Klosterzelgstrasse 2CH, Windisch 5210, Switzerland
[b] Operations Research and Logistics, Wageningen University and Research, Hollandseweg 1, Wageningen 6706 KN, The Netherlands
[c] Faculty of Engineering and Natural Sciences, Department of Mechanical Engineering, TC Ankara Yildirim Beyazit University, Ankara, Turkey
[d] Engineering and Technology Institute Groningen (ENTEG), Faculty of Science and Engineering, University of Groningen, Nijenborgh 4, Groningen 9747 AG, The Netherlands

HIGHLIGHTS

- Easy-to-manufacture design of flexible patterned wings with controllable lift.
- Optimized properties of flapping wings under manufacturing & operational constraints.
- Machine-learning-based finite-element optimization approach to tune design parameters.

GRAPHICAL ABSTRACT

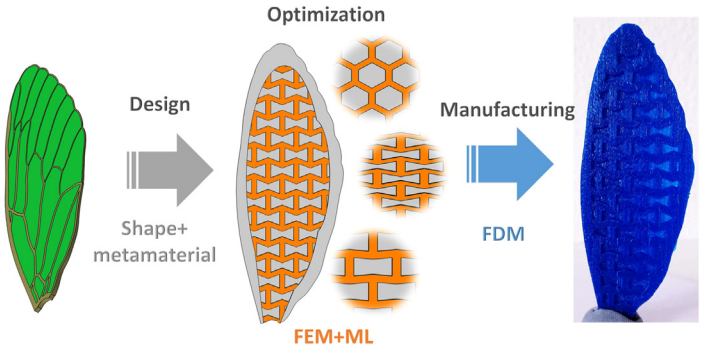

ARTICLE INFO

Article history:
Received 13 February 2022
Revised 20 April 2022
Accepted 28 April 2022
Available online 4 May 2022

Keywords:
Bio-inspired design
Artificial wing
Metamaterial
Lift
Surface pattern
3D-printing

ABSTRACT

Insect wings are formed by intricate combinations of flexible membranes and rigid veins; such a structure enables excellent flight performance, adaptability to aerodynamic forces, and biological functions. Comprehensive understanding of the interplay between wing patterning and flight dynamics has however not been achieved yet due to enormous variability of natural patterns and the extreme complexity of the modeling wing-air interactions. Therefore, the design of a pattern for artificial flexible wings is challenging. In contrast to other studies mimicking biological patterns of insect wings, we propose usage of metamaterials principles to enable controllable dynamics, and machine-learning techniques to solve a related multi-parameter design optimization problem. We demonstrate the advantages of this hybrid approach by finding practical patterns with improved target property – enhanced lift. The obtained designs were manufactured by means of a low-cost fused deposition modeling (FDM) 3D-printer from a single commercially available thermoplastic polyurethane (TPU) and revealed the required balance between the rigidity of metamaterial "veins" and the flexibility of the wing base. Extensions of our approach to other designs or analyses of other moving structures offer straightforward benefits in tackling a wide range of computationally complex aerodynamic and vibroacoustic problems.

1. Introduction

Fascinating mechanics of insect wings that can flap, rotate, and fold, have inspired numerous studies to reproduce similar functionalities in artificial wings [1]. Despite significant progress in

* Corresponding author.
E-mail address: a.o.krushynska@rug.nl (A.O. Krushynska).

https://doi.org/10.1016/j.matdes.2022.110709

understanding the fundamentals of the natural wings dynamics [2–4] and the development of manoeuvrable flying devices with flexible wings [5,6], the design strategies to achieve required flight performance for artificial flexible wings remain largely unavailable. Optimizing the wing structure requires solving a notoriously difficult non-linear problem of coupled air-wing interactions in a particular dynamic regime for each set of multiple parameters specifying the wing geometry [4,7,8]. The parameters space describes the variety of the wing pattern geometries formed by flexible membranes and rigid veins that define the wing aerodynamics [9] and acoustics [10]. Enormous diversity of natural patterns and a huge variability in shapes and sizes of insect wings [11] render exploring this space computationally infeasible. Therefore, the influence of the pattern geometry on the aerodynamic and acoustic properties of wings remains largely unexplored.

One of the first studies on the relationship between the venation pattern and the wing flexibility involved measuring the static flexural stiffness of wings of 16 insect species [9]. It was concluded that the leading-edge veins are responsible for a spanwise-chordwise anisotropy crucial for the flight. Inspired by these results, first artificial wings had a leading vein [6,12,13] and possibly a few internal veins [5,14]. Later, it was found that locally rigid and flexible regions substantially contribute to the variation of bending and torsion pressure distribution in a wing [15]. This observation was made by measuring the mechanical properties of artificial bio-mimetic (planar) wings having a natural wing morphology in the static regime. Recent works have reported on similar measurements under dynamic conditions and showed that the varying vein width alters the inertial resistance and enables the stiffness variation along the span of a wing, which enhances the lift capability [16–18]. The latest trend in the development of patterned artificial wings is to apply computer-assisted methods, e.g., generative design [19], in combination with the finite-element analysis.

To explore the space of wing pattern parameters, we focus on a computer-assisted design and propose a hybrid approach based on a combination of machine-learning techniques and the finite-element method. The pattern design relies on the concepts of metamaterials that provide unique opportunities to implement controllable dynamic and acoustic properties [20]. Metamaterials are man-made materials with tailorable characteristics mainly governed by the structure and arrangement of their building blocks rather than chemical constituents [21]. Precise control over the geometry and composition of building blocks enables, e.g., manipulating acoustic stress and sound waves by achieving perfect absorption [22,23], sound amplification [24–26], broadband vibration control [27,28], shape-morphing behavior [29], etc. Thus, in contrast to exploring the effects of available intricate natural patterns, we aim at optimizing the pattern design by considering a class of metamaterial patterns to achieve target flight characteristics.

For this purpose, we focus on widely-known periodic re-entrant honeycomb lattices that include regular honeycombs with isotropic mechanical properties [30] and irregular honeycombs exhibiting highly anisotropic response and a zero or negative effective Poisson's ratio [31]. These lattices described by a few geometric parameters cover a broad range of possible patterns and enable us to get insights into the advantages of various patterns for artificial flexible wings. To reach this goal, we develop a two-step numerical approach that allows studying the influence of the pattern on the flight characteristics of a wing and optimising the pattern design in terms of a desired property. This work considers the "lift" functional as an example of a target characteristic; other examples including the sound level or maximum stress functional (see Ref. [32] for details) can also be used in the proposed procedure, but are not considered here, for brevity. The proposed approach combines the advantages of the finite-element method capable of solving a non-simplified three-dimensional air-wing interaction problem with machine-learning algorithms that enable substantial reduction in the number of computationally costly simulations, which are typical for vibroacoustic studies [33–37]. Importantly, our approach delivers feasible optimized designs of artificial wings satisfying manufacturing constrains imposed by a low-cost fused deposition modeling (FDM) 3D-printing from commercial materials. This ensures its direct applicability to the design of flexible wings for (micro-) robotic flying devices.

2. Model and flight conditions

We consider a model of an artificial wing with the shape of a natural dragonfly wing that is cambered out-of-plane similar to its natural counterpart (Fig. 1, left). The top surface of the wing is covered by a regular periodic pattern surrounded by an exterior "vein". The pattern is a re-entrant honeycomb lattice occupying 90% of the wing surface (Fig. 1, center). Such a lattice provides a broad range of effective mechanical properties governed by the following five geometric parameters (see Fig. 1, right, for details):

- out-of-plane thickness th;
- width of the beams w;
- "narrowing" ratio $r = b/a$;
- scale factors s_x and s_y along the x- and y-directions, respectively, to control the pattern elongation.

The in-plane dimensions of the wing are 30.5 mm along the y-axis (span-wise), 80 mm along the x-axis (cord-wise), and the out-of-plane thickness th gradually decreases from 1.8 mm (at the leading vein) to 0.4 mm along the span-wise direction. These correspond to a two-times larger and four-times thicker wing as compared to its natural counterpart [38]. The initial parameters of the re-entrant lattice are $th = 2$ mm, $w = 0.8$ mm, $r = 0.4$, and $s_x = s_y = 1$ (see Fig. 1).

We assume that the wing is made from a single material in agreement with the structure of natural wings made from chitin [9]. This imposes a strict requirement on the choice of the base material that needs to behave as flexible and rigid, simultaneously. To satisfy this requirement, we choose for a durable, chemically resistant, and flexible thermoplastic polyurethane (TPU) as a base.

Aiming at low-cost manufacturing of the proposed wings, we consider commercially available Kimya TPU-R filament (2.85 mm) for FDM printing with mass density $\rho = 1159$ kg/m^3, Young's modulus $E = 90$ MPa, and Poisson's ratio $\nu = 0.48$, according to an official data sheet. The 3D-printed TPU can show flexible or rigid behavior depending on the number of printed layers. To demonstrate this, we manufactured five rectangular samples of identical in-plane dimensions 30.3 mm by 5.5 mm and with 2, 4, 6, 8, and 10 printed layers (of thickness 0.2 mm) in the out-of-plane direction (Fig. 2b). The length of the samples is almost equal to the span-wise direction of the wing, while the width is adjusted to that of a clamp. The samples were produced by means of the FDM 3D printer Ultimaker 3.0. The mentioned thicknesses cover the range of the thickness values of the wing. The samples were fixed by a clamp (Fig. 2c) and statically loaded by suspended weight of 38 g (Fig. 2d). Note that this setup serves the demonstration purposes only and has no relation to the wing's dynamics. As can be seen, the 2-mm thick (10-layered) sample reveals a comparatively rigid response to the static loading, while the 0.4-mm thick sample is highly flexible. Therefore, by changing the number of printed layers, we can control the flexibility of a 3D-printed TPU structure that enables considering a metamaterial pattern on the wing surface as a reinforcement of a flexible base wing.

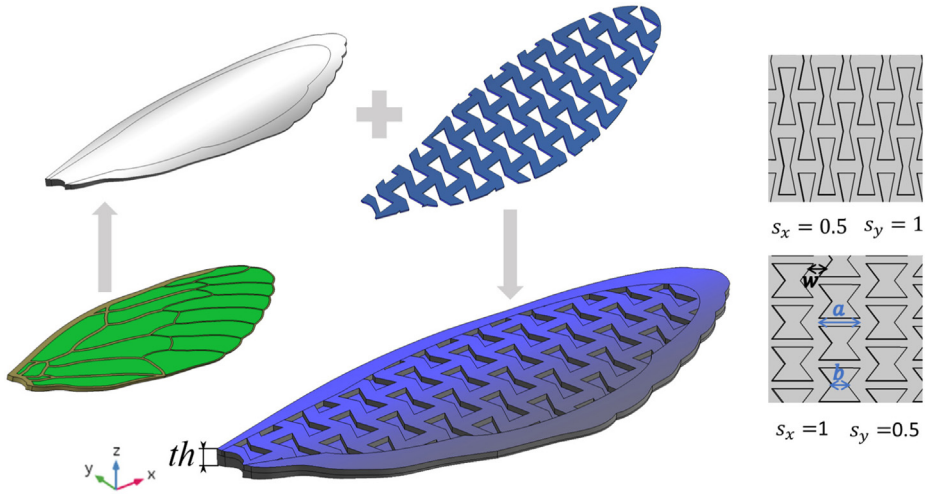

Fig. 1. Design scheme for an artificial flexible wing with a metamaterial pattern: (left) natural dragonfly wing serves as inspiration for the shape and camber of the base (unpatterned) wing; (center) re-entrant honeycomb lattice of a uniform thickness is added to the top surface of the base wing and forms the final design; (right) illustration of the scaling of the pattern along the span-wise and chord-wise directions.

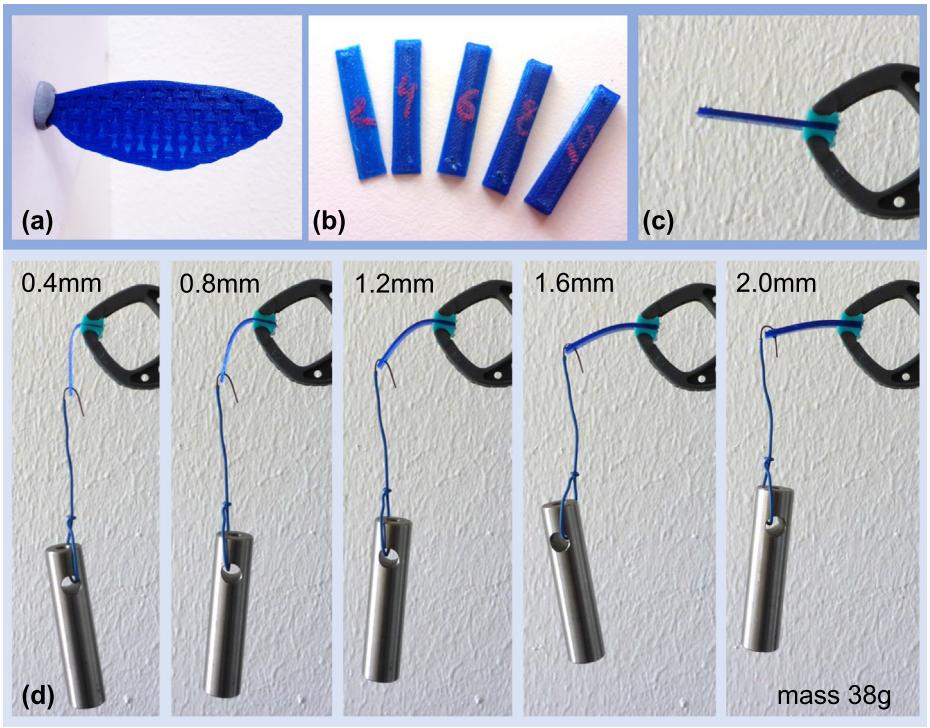

Fig. 2. (a) FDM-printed TPU wing with a re-entrant honeycomb pattern; (b) TPU-printed samples (30.3mmx5.5 mm) with 2, 4, 6, 8 and 10 printed layers; (c) the clamped unloaded sample; (d) deflections of the samples under a static loading by the weight of 38 g that demonstrate the material flexibility governed by the number of printed layers (the numbers indicate the thickness of a sample).

The designed wing is also manufactured by the same (dual-nozzle) 3D-printer from Kimya TPU-R as a base and a water-soluble PVA (Ultimaker PVA, 2.85 mm) as a support with the printing resolution of 0.1 mm (Fig. 2a). The support is needed to keep the cambered shape of the wing. Hence, the proposed wing design is realizable. The quality and durability of 3D-printed TPU wings with a honeycomb pattern have already been studied experimentally in Ref. [32]. Note that TPU can also be used in selective laser sintering (SLS) and multi jet fusion (MJF) additive manufacturing [39]. These are more advanced production techniques with a superior resolution of printed layers (starting from 100 μm) that can further increase the quality of the wings.

3. Problem statement and analysis details

The dynamics of a flexible wing implies its large nonlinear deformations influenced by induced variations of acoustic pressure in the surrounding air. This results in a nonlinear fully-coupled fluid–structure interaction problem in a three-dimensional setting that is challenging even for modern computers. Solving this problem and understanding the effects of a pattern on aerodynamic characteristics of a wing becomes computationally feasible only if the number of parameters is reduced. For this purpose, we choose the five parameters of the proposed wing pattern as design variables and consider simple flight conditions, with a minimum

number of parameters, though preserving the full complexity of three-dimensional wing-air coupled dynamics.

In particular, since the wing is cambered, the lift can be generated at a zero angle of attack. Hence, we ignore the variation of the angle of attack from the consideration [10] by noting that our solution approach is also applicable at a non-zero angle of attack. Next, we consider a flapping flight implying up–down wing motions without forward movement and exclude any external forces (e.g., wind). Finally, we also neglect excitation mechanisms of the wing, its fixation conditions, interactions with other possible parts of a flying device, etc. These also influence the wing characteristics significantly [7], but are more relevant when developing a specific flying device that goes beyond the scope of this study.

At the beginning of a flapping cycle, the wing is in a horizontal position with the mid-plane in the *Oxy* plane (Fig. 3, center), the chord direction parallel to the *x* axis. The flapping motions are excited by torque induced by out-of-plane rotation at the leading edge and the line indicated in blue in Fig. 3a by means of the vertical displacement:

$$u_z = A_0 \sin(2\pi f^e t), \tag{1}$$

where f^e is the flapping frequency; A_0 is the stroke amplitude. Note that at distance D from the base (shown in green in Fig. 3a) to the leading edge is fixed to exclude in-plane translational motion. The described flapping conditions are close to those of a hovering flight of insects [40].

The flapping motion of the wing under specified conditions induces laminar flows of air with small Reynolds numbers (< 3). This enables us to neglect air compressibility [41] and to describe the dynamics of the surrounding air as that of a Newtonian fluid governed by the classic viscous incompressible Navier–Stokes equations:

$$\frac{\partial \mathbf{u_a}}{\partial t} + \mathbf{u_a} \cdot \nabla \mathbf{u_a} = -\frac{1}{\rho_a}\nabla p + \frac{\mu}{\rho_a}\nabla^2 \mathbf{u_a}, \tag{2}$$

$$\nabla \cdot \mathbf{u_a} = 0. \tag{3}$$

Here $\mathbf{u_a}$ is a three-dimensional velocity vector for air, ρ_a is the air density, μ is the dynamic viscosity, and p is the pressure.

The air domain in the model is represented by a half ellipsoid with axes 0.05 m×0.1 m×0.08 m enclosing the wing (Fig. 3b). The normal component of outgoing total pressure at the outer boundaries, $p\mathbf{I} - \mu(\nabla \mathbf{u_a} + (\nabla \mathbf{u_a})^T)$, is set equal to atmospheric pressure p_0 with the aim to reduce the influence of boundaries. At the interfaces with the wing, we apply no-slip boundary condition $\mathbf{u_a} = \mathbf{u}_{tr}$, where $\mathbf{u}_{tr}$ indicates the translational velocity of the wing. The material properties of air are standard as for 20°C.

The flapping flexible wing experiences large deformations that should satisfy the equations of motion in terms of displacement vector $\mathbf{u_w}$:

$$\rho \frac{\partial^2 \mathbf{u_w}}{\partial t^2} = \nabla \cdot (FS)^T, \tag{4}$$

where ρ is the material density of the wing, F is the deformation gradient, S is the second Piola–Kirchhoff stress tensor. At the initial time, the displacements and velocities equal to zero.

To capture the interactions between the flapping wing and the air, we use the fluid–structure interface coupling implemented in the COMSOL Multiphysics. This coupling is realized based on the arbitrary Lagrangian–Eulerian approach considering acoustic pressure variations due to wing deformations, the influence of induced acoustic pressure and its variations caused by the wing motions.

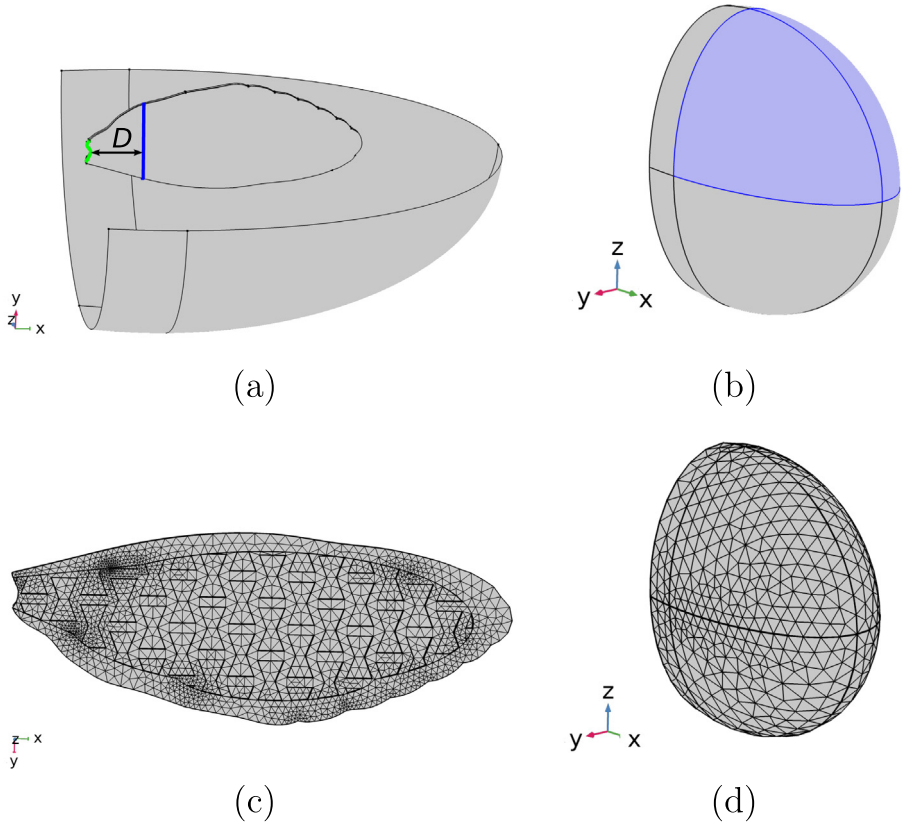

Fig. 3. (a) Flapping motions are induced by a harmonic loading at the edge marked in blue and by fixing all displacements at the edge marked in green. (b) Half-ellipse of air surrounding the wing with the top surface marked in blue. (c) Finite-element mesh of the wing. (d) Finite-element mesh of the air domain.

Specifically, the air exerts a total force on the wing opposite to the reaction force on the air,

$$\mathbf{f} = \mathbf{n} \cdot \left\{ -p\mathbf{I} + \left(\mu(\nabla \mathbf{u_a} + (\nabla \mathbf{u_a})^T) - \frac{2}{3}\mu(\nabla \cdot \mathbf{u_a})\mathbf{I} \right) \right\} \quad (5)$$

with $\mathbf{n}$ indicating the outward normal to the wing boundary and $\mathbf{I}$ being the identity matrix. Note that the air dynamics is analyzed in the spatial (deformed) frame, while the wing motions and corresponding interfaces are defined in the material (undeformed) frame, that requires to introduce the force transformation:

$$\mathbf{F} = \mathbf{f} \cdot \frac{dv}{dV}, \quad (6)$$

where dv and dV are the mesh elements for the spatial and material frames, respectively. The other types of coupling are implemented through velocity $\partial \mathbf{u_w}/\partial t$ playing the role of a moving wall for the air domain. The coupled equations in this formulation have been successfully applied to model fluid–structure interactions in flapping and forward flights and proved an excellent accuracy in the absence of turbulent flows, see, e.g., Refs. [8,42–44].

In the simulations, we use a free tetrahedral mesh with maximum (average) element sizes of 0.0042 (0.0025) m and 0.022 (0.011) m for the wing (air) domain with a cubic Lagrange discretization (Figs. 3c,d). To resolve thin air layers near the wing-air interfaces, we consider at least two layers of a finer mesh. Hence, the final mesh contains $1.0 - 1.2 \times 10^5$ domain elements, $6.5 - 7.0 \times 10^3$ boundary elements, and $1.5 - 2.0 \times 10^3$ edge elements depending on the pattern design. The sensitivity analysis revealed that this and finer (two times smaller) meshes result in the pressure and deformation values that differ by less than 1%. It validates the appropriateness of the mesh and its applicability for the parametric studies described above.

The fluid–structure interaction problem is solved in the time domain for the time step governed by the backward differentiation formula. The fixed time step of $1/60 \cdot f^e$ s is obtained by considering the structural transient behavior for inertial terms with the limit of maximum excitation frequency $f^e = 25$ Hz. The governing equations are discretized by cubic Lagrange elements. The pressure variations are stabilized within about 0.15 s and 0.3–035 s at frequencies far and near resonances, respectively, that requires the simulation time of about 1 h (Processor Intel® Xeon® Gold 5118 CPU, 2.30 GHz with 2 real cores, 64 virtual cores; total (used for the simulation) RAM: 128 GB (15 GB); 64-bit operational system).

4. Multi-dimensional problem analysis

The five parameters of the lattice form a five-dimensional design space, and enable an enormous variety of possible patterns. To explore this space and ensure a fair comparison of different designs, we need to distinguish the patterns sharing common characteristics from the others. For this, we propose to consider the first eigenfrequency of the wing as a common characteristic, as it can be directly linked to a resonant flapping flight ensuring similar flight conditions for wings with different patterns. Our previous results show that 3D-printed TPU wings are promising candidates for resonant flapping flights as revealing no damage under long-term resonant excitation [32].

The finite-element eigenfrequency analysis (the ARPACK solver of the Comsol Multiphysics) shows that many of the patterned wings have the first eigenfrequency around 25 Hz. Hence, we assign the frequency of flapping motions to be $f^e = 25$ Hz and aim at finding all possible combinations for the pattern parameters that correspond to the first eigenfrequency of the wing f^1 close to f^e with the tolerance ± 1 Hz.

4.1. Analysis of the eigenfrequency

In other words, our *first goal* is to find a region in the 5-dimensional space of the pattern parameters for which the difference $W^d = |f^1 - f^e|$ does not exceed the given threshold value of 1.0 Hz. Note that f^1, respectively W^d, is essentially a functional of five variables: th, s_x, s_y, r, w.

Despite that the eigenfrequency calculation is relatively fast on its own, the exploration of the five-dimensional space requires a huge number of these calculations, resulting in a prohibitively large overall computational effort. To overcome this, we employed machine learning techniques to partially replace relatively time consuming eigenfrequency calculations by substantially faster machine-learning based 'predictions'. At a high level, our framework can be expressed as the following Algorithm 1.

Algorithm 1.

STEP 1: collect a small number of data points by calculating eigenfrequencies for a small set of parameter combinations;
STEP 2: using the available data points, train an 'oracle' that can 'predict' the W^d-value for any given combination of parameters;
STEP 3: use an 'oracle' to find the promising region in the 5-dimensional space, i.e. a region where $W^d \leqslant 1.0$;
STEP 4: extend the set of data points by calculating eigenfrequencies for more parameter combinations from the promising region and repeat Step 2. End.

In the first step, 200 points (parameter combinations) were randomly sampled from the parameter space, and the corresponding eigenfrequencies were calculated. The parameter space was restricted to the following ranges: $0.2 \leqslant th \leqslant 1.5$ mm, $0.5 \leqslant s_x \leq 1.5, 0.5 \leqslant s_y \leq 1.5, 0.4 \leqslant r \leqslant 1.0, 0.8 \leqslant w \leqslant 2$ mm. These ranges are based on practical considerations. For example, parameter w has a lower bound of 0.8 mm due to the diameter of the printing nozzle, and hence the minimum physically possible double wall thickness for the (arguably) most common 0.4 mm nozzles. Parameter r is bounded to prevent contact (intersection) of the opposite walls which would modify the topology of the pattern.

In Step 2, several regression models available in Matlab were trained. These models provided the following R-square values: 'quadratic' – 0.944, 'purequadratic' – 0.862; 'interactions' – 0.884, and 'linear' – 0.773. The 'quadratic' regression model with the best R-square value was selected for a role of the 'oracle'.

The 'oracle' was used to estimate the promising region, i.e., a region in the parameters space where the predicted value of W^d is bounded by the threshold of 1.0 Hz. Further 1800 samples from the promising region were randomly generated, their eigenfrequencies were calculated and used to train the regression model (Step 4). At this stage, we tried again all available in Matlab types of regression and the one giving the best R-squared value of 0.941 (RMSE = 0.295) is the quadratic regression, given in Table 1.

Fig. 4 illustrates the discrepancy between the data points and the response of the regression model. The outliers can be explained by the inaccuracy of the geometry reconstruction for various values of design parameters and dependency on COMSOL geometry postprocessing procedures. The cross-validation of the regression model was performed by splitting the data points into 5 subsets and comparing the model outcomes. This was done via the built-in Matlab tool – Regression Learner App.

In order to gain insights into the influence of the parameters on W^d, we considered a number of two-dimensional reductions of the

Table 1
Coefficients for the quadratic regression model to approximate W^d. The first column corresponds to the linear part of the regression, the diagonal corresponds to the quadratic terms, other coefficients correspond to mixed products of variables: $0.248 \cdot 10^2 - 0.787 \cdot 10^4 \cdot th + 0.231 \cdot 10^8 \cdot th^2 + \ldots + 0.472 \cdot 10^6 \cdot w^2$.

	1	th	s_x	s_y
1	0.240e+02			
th	−0.787e+04	0.231e+08		
s_x	0.166e+00	0.118e+05	−0.163e+01	
s_y	−0.610e+00	-0.544e+04	0.154e−01	0.132e+01
r	−0.270e+01	0.808e+04	0.122e+00	−0.822e+00
w	−0.153e+04	0.125e+07	0.108e+04	−0.504e−01

	r	w
r	0.822e+00	
w	0.213e+03	0.472e+06

original five-dimensional functional $W^d(th, s_x, s_y, r, w)$, obtained by selecting two dimensions and replacing W^d by a minimum value over the remaining three dimensions. For example, a reduction of $W^d(th, s_x, s_y, r, w)$ to the (th, s_x)-space is defined as follows:

$$W^d_{th,s_x}(x, y) = \min_{s_y,r,w} W^d(x, y, s_y, r, w) \tag{7}$$

Reduced functionals can be plotted as two-dimensional height maps for the purposes of visual inspection and further analysis. Note that a similar reduction can be applied not to W^d itself but to its approximation resulting from a regression model ('oracle'). In the rest of this paper, speaking about the reduced functionals we mean their approximations.

The two-dimensional maps resulting from the regression model (see Table 1) are shown in Fig. 5 (for the most interesting pairs of parameters) and in Appendix A.

Based on the obtained figures, we conclude that parameter s_x has the largest impact on the eigenfrequency of the wing, and that for the lattice thickness $th > 4.5 \cdot 10^{-4}$ it is not possible to approach the target value of 25 Hz for any combination of other parameters. The remaining parameters have a limited impact in a sense that after fixing any of them to some value (within the considered ranges) it is possible to find a suitable combination of other parameters to ensure $W^d \leqslant 1$.

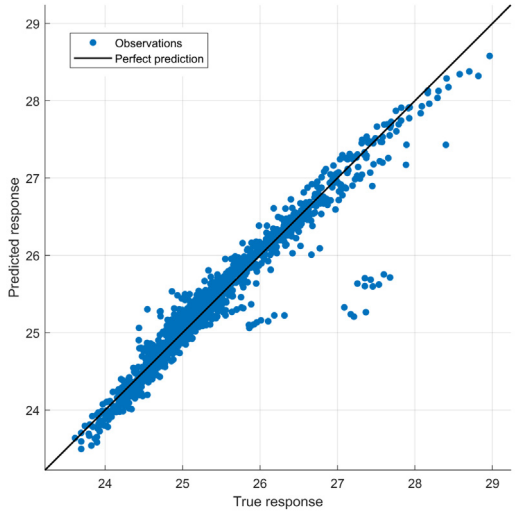

Fig. 4. Accuracy of the eingenfrequency prediction by the quadratic regression model for 1000 samples.

4.2. Analysis of lift

Knowing the patterns leading to eigenfrequencies close to 25 Hz, we continue to our *second goal* of finding the patterns with a maximum lift property. We estimate lift W^L as a time averaged sum of the pressure integrals over the top and bottom surfaces of the wing:

$$W^L = -\underset{[t_s,t_f]}{\mu}\left(\int_{A_{top}} pdA + \int_{A_{bot}} pdA\right), \tag{8}$$

where t_s and t_f are the starting and final moments of time indicating the period of stabilised flapping motion, i.e. excluding the initial transient phase. The minus-sign is introduced for the sake of uniformity: smaller values are preferable for both W^d and W^L. The lift is calculated by numerically solving a three-dimensional fluid–structure interaction problem described in Section 3. More details about the lift generation mechanism and the analysis of corresponding conditions can be found in our previous study [32].

In order to estimate the lift for a given parameters combination, the corresponding eigenfrequency value is needed. The necessary eigenfrequency values were calculated using the regression from Table 1.

Our study of the lift follows the framework described in Section 4.1 and Algorithm 1 in particular. However, due to a substantially higher complexity of solving the fluid–structure interaction problems (compared to the problem of calculating eigenfrequencies), this part of the study is more limited in the amount of data we could collect. We started with 20 data points; after training a regression model, 180 additional points from the most promising parameters region were evaluated. The resulting dataset is used to train available in Matlab regression models mentioned above. The best performing is again the quadratic model with R-square of 0.952, RMSE of $3.1 \cdot 10^{-7}$, and the coefficients given in Table 2.

Fig. 6 illustrates discrepancies between the data points and the response of the regression model. The cross-validation of the regression model was performed by splitting the data points into 3 subsets and applying Regressions Learner App from Matlab.

The results of this analysis can be visualised via 2-dimensional maps described in Section 4.1, see Fig. 7 and Appendix A. The maps show that, similar to the eigenfrequency results, parameters th and s_x have the largest impact on the lift of the wing. Other parameters are less relevant in a sense that it is possible to give any individual parameter an arbitrary value and select the values of the other parameters to reach the highest lift. Note that the color scale differs per map in Fig. 7, so the variability of the (r, w)-reduced lift functional is much less than that of, for example, (th, s_x)-reduced functional.

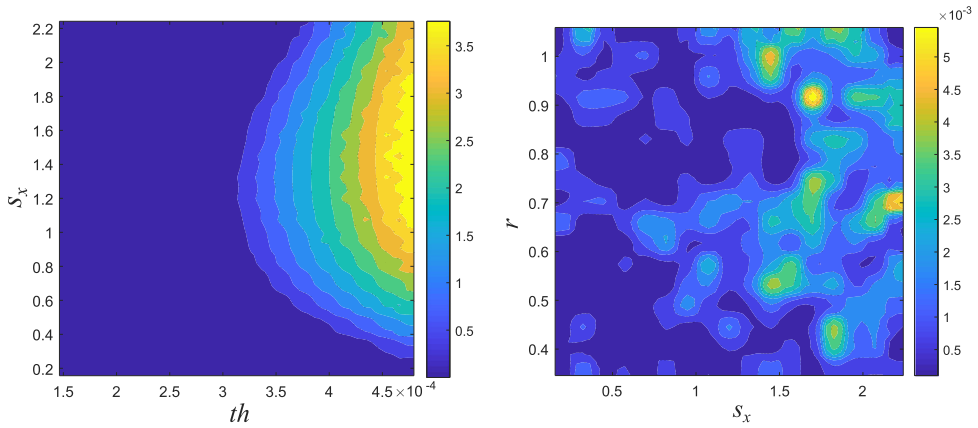

Fig. 5. W^d-maps for some pairs of parameters in the eigenfrequency analysis. Note a significant difference between the colour scale in the two maps.

Table 2
Coefficients for the quadratic regression model to approximate W^L. The first column corresponds to the linear part of the regression, the diagonal corresponds to the quadratic terms, other coefficients correspond to mixed products of variables: $0.259 \cdot 10^{-4} - 0.18 \cdot th + 0.16 \cdot 10^3 \cdot th^2 + \ldots + 0.187 \cdot 10^{-5} \cdot (f^1)^2$.

	1	th	s_x	s_y
1	0.259e−04			
th	−0.180e+00	0.160e+03		
s_x	−0.198e−04	0.354e−01	0.292e−05	
s_y	0.623e−05	−0.686e−02	−0.158e−05	−0.336e−06
r	−0.692e−05	0.124e−01	0.348e−05	−0.333e−06
w	−0.105e−01	1.991e+01	0.164e−02	−0.165e−03
f^1	0.604e−05	−0.136e−01	−0.189e−05	0.108e−05

	r	w	f^1
r	0.401e−06		
w	0.466e−03	0.520e+00	
f^1	−0.685e−06	−0.104e−02	0.187e−05

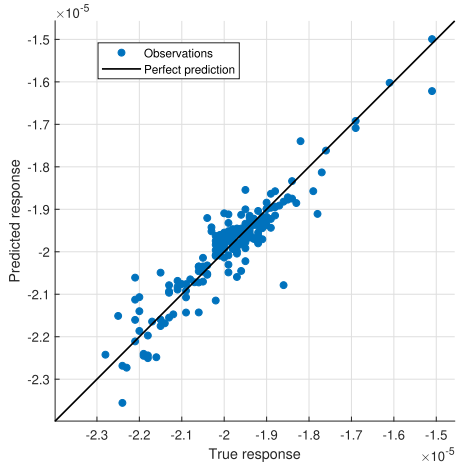

Fig. 6. Prediction of the lift response objective.

4.3. Multiobjective analysis

A realistic wing design problem is of a multiobjective nature and requires trade-offs between conflicting goals (e.g. durability vs. weight or lift vs. noise level). However, our two goals (low W^d, high W^L) do not conflict in a sense that there is a region in the parametric space where both goals are satisfied. To illustrate this, we use an 'aggregate' representation of 2-dimensional maps of both goals. The aggregate maps are based on the following functional W^A:

$$W^A(.,.,.,.,.) =$$

$$\begin{cases} W^L(.,.,.,.,.), & \text{if } (W^d(.,.,.,.,.) \geqslant 1)\,\text{OR}\,(s_x \cdot w \geqslant 0.4)\,\text{OR}\,(s_y \cdot w \geqslant 0.4) \\ -1.8 \cdot 10^{-5}, & \text{otherwise} \end{cases} \tag{9}$$

Note that the aggregate functional incorporates also practical constraints: a lower bound on the thickness of the walls in the pattern. In a similar way, other practically relevant restrictions may be included into the analysis.

The 2-dimensional maps of W^A are given in Fig. 8 and Appendix A. As seen from the figure, an interesting effect of aggregating two goals and imposing the restrictions lies in the fact that the desired combinations of parameters are now restricted to bounded regions in the maps. This means that "good" parametric configurations are not extreme and extending our study to broader ranges of parameters is not required.

The final stage in our analysis relates to the interplay between the first eigenfrequency f^1 of the wing and the lift it generates. One can expect that the highest lift can be obtained at $f^1 = f^e = 25$ Hz, equivalently $W^d = 0$. However, our computational results suggest that this is not completely true (see Fig. 9), as the highest lift (respectively, lowest W^L) is obtained at f^1 slightly above f^e. We explain this effect by the wing-air interaction that changes the eigenfrequencies of the wing. Recall that our eigenfrequency calculations are based purely on the wing properties and disregard any influence of the environment, while the lift calculations consider wing-air interactions (see Section 3).

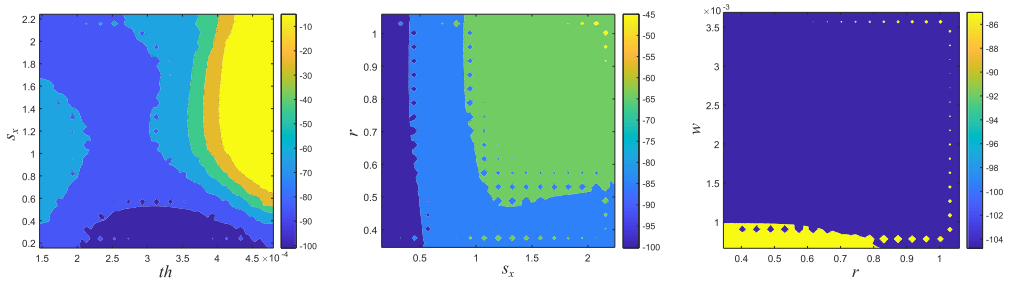

Fig. 7. Lift maps for some pairs of parameters (W^L values are normalised).

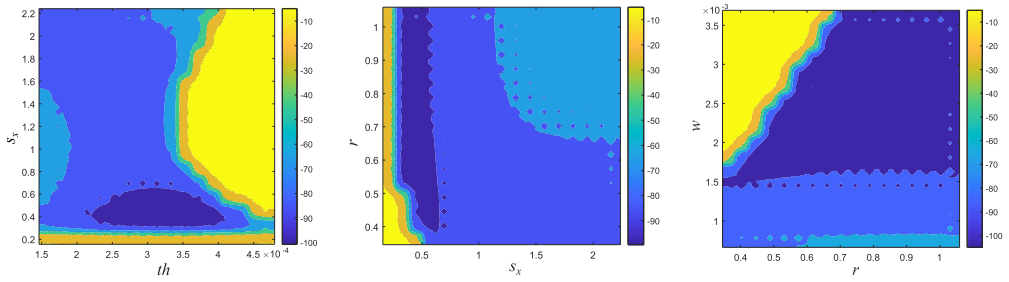

Fig. 8. Aggregate maps for several parameters combinations (the lift values are normalised to interval $[-100; 0]$).

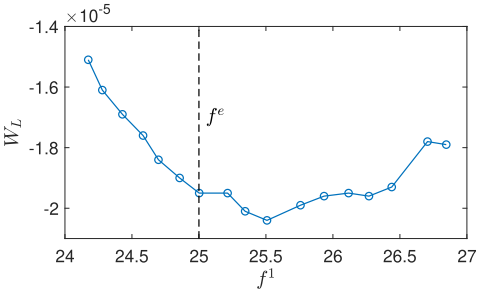

Fig. 9. Lift W^L vs. eigenfrequency f^1 of the wing.

To conclude this section, desired configurations of the 3D-printed structure can be found for multiple criteria and set of design variables using a combination of FEM and machine learning methods. Note that our approach goes beyond optimisation, i.e., finding a single 'best' pattern or combination of parameters. Instead, our maps illustrate the parametric regions with desired properties and thus give information about how sensitive the performance is to the value of any parameter involved.

5. Conclusions

In this paper we developed and numerically validated a hybrid approach to the design of artificial flexible wings that combines FE-modelling and machine learning techniques in a coherent way. By considering a class of metamaterial patterns used in the wing design, we show that multi-parameter analysis problems can be efficiently tackled in a realistic setting. In particular, using two example characteristics (eigenfrequency and lift) and some structural restrictions (limited width of structural elements), we generate insights into the effect of parameters at a cost of a reasonable computation effort.

For the considered class of patterns and performance criteria, it was found that the thickness and longitudinal scaling of the pattern (i.e, the pattern anisotropy in the chord-wise direction) are the most crucial parameters, while others play a secondary role: a specific value of any of them can be 'compensated' by a more careful selection of other parameters to achieve the desired qualities of the wing. It was also found that the 'best' parametric settings are limited to bounded regions in the interior the considered ranges.

It is worth mentioning that out approach can be naturally extended to other classes of metamaterial and even biomimetic patterns (respectively, other parameterisations), as well as to other design and analysis problems (not only wings, but also other moving structures). Also, our approach is flexible in a sense that manufacturing/operational/etc. restrictions can be taken in consideration, without noticeably increasing the computational complexity of the analysis.

Declaration of Competing Interest

The authors declare that they have no known competing financial interests or personal relationships that could have appeared to influence the work reported in this paper.

References

[1] W. Shyy, C.-K. Kang, P. Chirarattananon, S. Rai, H. Liu, Aerodynamics, sensing and control of insect-scale flapping-wing flight, Proc. R. Soc. A 472 (2016) 20150712.
[2] R.J. Wootton, R.C. Herbert, P.G. Young, K.E. Evans, Approaches to the structural modelling of insect wings, Phil. Trans. R. Soc. Lond. B 358 (2003) 1577–1587.
[3] Z.J. Wang, Dissecting insect flight, Annu. Rev. Fluid Mech. 37 (2005) 183–210.
[4] M. Sun, Insect flight dynamics: Stability and control, Rev. Mod. Phys. 86 (2014) 615.
[5] R.J. Wood, The First Takeoff of a Biologically Inspired At-Scale Robotic Insect, IEEE Trans. Robotics 24 (2) (2008) 341–347.
[6] L.-J. Yang, The micro-air-vehicle golden snitch and its figure-of-8 flapping, J. Appl. Sci. Engng. 12 (2012) 197–212.
[7] F.O. Lehmann, When wings touch wakes: understanding locomotor force control by wake wing interference in insect wings, J. Exp. Biol. 211 (2008) 224–233.
[8] Z.J. Wang, Two Dimensional Mechanism for Insect Hovering, Phys. Rev. Lett. 85 (10) (2000) 2216–2218.

[9] S.A. Combes, T.L. Daniel, Flexural stiffness in insect wings II. spatial distribution and dynamic wing bending, J. Exp. Biol. 206 (2003) 2989–2997.
[10] Y. Bae, Y.J. Moon, Aerodynamic sound generation of flapping wing, J. Acoust. Soc. Amer. 124 (2008) 72–81.
[11] J. Hoffmann, S. Donoughe, K. Li, M.K. Salcedo, C.H. Rycroft, A simple developmental model recapitulates complex insect wing venation patterns, Proc. Natl. Acad. Sci. U.S.A. 115 (40) (2018) 9905–9910.
[12] Q. Zhu, Numerical Simulation of a Flapping Foil with Chordwise or Spanwise Flexibility, AIAA J. 45 (10) (2007) 2448–2457.
[13] T. van Truong, Q.-V. Nguyen, H.P. Lee, Bio-Inspired Flexible Flapping Wings with Elastic Deformation, Aerospace 4 (3) (2017) 37.
[14] L. Zhao, Q. Huang, X. Deng, S.P. Sane, Aerodynamic effects of flexibility in flapping wings, J.R. Soc, Interface 7 (2010) 485–497.
[15] J.K. Shang, S.A. Combes, B.M. Finio, R.J. Wood, Artificial Insect Wings of Diverse Morphology for Flapping-Wing Micro Air Vehicles, Bioinsp. Biomim. 4 (3) (2009) 036002.
[16] J.E. Rubio, U.K. Chakravarty, Experimental structural dynamic measurements of an artificial insect-sized wing biomimicking a crane fly forewing, Acta Mech. 230 (2019) 4273–4286.
[17] X. Li, C. Guo, Microstructure and material properties of hind wings of a bamboo weevil Cyrtotrachelus buqueti (Coleoptera: Curculionidae), Microsc. Res. Tech. 82 (2019) 1102–1113.
[18] N. Chitsaz, K. Siddiqui, R. Marian, J. Chahl, An experimental study of the aerodynamics of micro corrugated wings at low Reynolds number, Exp. Therm. Fluid Sci. 121 (2021) 110286.
[19] H. Isakhani, N. Bellotto, Q. Fu, S. Yue, Generative design and fabrication of a locust-inspired gliding wing prototype for micro aerial robots, J. Comput. Des. Eng. 8 (5) (2021) 1191–1203.
[20] R.V. Craster, S. Guenneau, Acoustic Metamaterials: Negative Refraction, Imaging, Lensing and Cloaking, Springer, 2013.
[21] A.O. Krushynska, A.S. Gliozzi, A. Fina, D. Krushinsky, D. Battegazzore, M.A. Badillo-Ávila, M. Acuautla, S. Stassi, C. Noè, N.M. Pugno, F. Bosia, Dissipative Dynamics of Polymer Phononic Materials, Adv. Funct. Mater. 31 (30) (2021) 2103424.
[22] N. Jiménez, W. Huang, V. Romero-García, V. Pagneux, J.P. Groby, Ultra-thin metamaterial for perfect and quasi-omnidirectional sound absorption, Appl. Phys. Lett. 109 (2016) 121902.
[23] X. Wang, X. Luo, H. Zhao, Z. Huang, Acoustic perfect absorption and broadband insulation achieved by double-zero metamaterials, Appl. Phys. Lett. 112 (2018) 021901.
[24] Y. Chen, H. Liu, M. Reilly, H. Bae, M. Yu, Enhanced acoustic sensing through wave compression and pressure amplification in anisotropic metamaterials, Nat. Commun. 5 (2014) 5247.
[25] Z. Liang, J. Li, Extreme acoustic metamaterial by coiling up space, Phys. Rev. Lett. 108 (2012) 114301.
[26] A.O. Krushynska, F. Bosia, M. Miniaci, N.M. Pugno, Spider web-structured labyrinthine acoustic metamaterials for low-frequency sound control, New J. Phys. 19 (10) (2017) 105001.
[27] N. Jiménez, V. Romero-García, V. Pagneux, J.P. Groby, Rainbow-trapping absorbers: Broadband, perfect and asymmetric sound absorption by subwavelength panels for transmission problems, Sci. Rep. 7 (1) (2017) 13595.
[28] A.O. Krushynska, A. Amendola, F. Bosia, C. Daraio, N.M. Pugno, F. Fraternali, Accordion-like metamaterials with tunable ultra-wide low-frequency band gaps, New J. Phys. 20 (7) (2018) 073051.
[29] A.E.M. Schmerbauch, A.O. Krushynska, A.I. Vakis, B. Jayawardhana, Modular Kirigami Arrays for Distributed Actuation Systems in Adaptive Optics, Phys. Rev. Appl. 17 (4) (2022) 044012.
[30] L.J. Gibson, M.F. Ashby, Cellular Solids, 2nd Ed., Cambridge University Press, Cambridge, 1997.
[31] J.B. Choi, R.S. Lakes, Non-linear properties of polymer cellular materials with a negative Poisson's ratio, J. Mater. Sci. 27 (1992) 4678–4684.
[32] I. Zhilyaev, N. Anerao, A.G.P. Kottapalli, M. Cihat Yilmaz, M. Murat, M. Ranjbar, A.O. Krushynska, Fully-printed metamaterial-type flexible wings with controllable flight characteristics, Bioinspir. Biomim. 17 (2022) 025002.
[33] M. Ranjbar, St. Marburg, Fast Vibroacoustic optimization of mechanical structures using artificial neural networks, Int. J. Mech. Eng. 1–3 (2013) 64–68.
[34] G. Hussain, M. Ranjbar, S. Hassanzadeh, Trade-off among Mechanical Properties and Energy Consumption in Multi-Pass Friction Stir Processing of Al 7075–T651 Alloy Employing Hybrid Approach of Artificial Neural Network and Genetic Algorithm, Proc. IMechE Part B: J. Engineering Manufacture 231 (1) (2015) 129–139.
[35] M. Ranjbar, M. Gharooni Saffar, A Sensitivity Analysis on Application of Artificial Neural Networks in Structural Acoustics, J. Robotic and Mechatronic Systems 1 (2) (2016) 23–26.
[36] M. Ranjbar, L. Boldrin, F. Scarpa, S. Niels, S. Patsias, Vibroacoustic optimization of anti-tetrachiral and auxetic hexagonal sandwich panels with gradient geometry, Smart Mater. Struct. 25 (5) (2016) 054012.
[37] M.S. Mazloomi, M. Ranjbar, L. Boldrin, F. Scarpa, S. Patsias, N. Ozada, Vibroacoustics of 2D Gradient Auxetic Hexagonal Honeycomb Sandwich Panels, Compos. Struct. 187 (2018) 593–603.
[38] U. Oberdörster, P.R. Grant, Predator foolhardiness and morphological evolution in 17-year cicadas (Magicicada spp.), Biol. J. Linn. Soc. 90 (2007) 11–13.
[39] A.O. Krushynska, N. Anerao, M.A. Badillo-Ávila, M. Stokroos, M. Acuautla, Arbitrary-curved waveguiding and broadband attenuation in additively manufactured lattice phononic media, Mater. Design 205 (2021) 109714.
[40] A.K. Brodsky, The Evolution of Insect Flight, Oxford University Press, Oxford, 1994.
[41] W.P. Graebel, Engineering Fluid Mechanics, Taylor & Francis, 2001. 16.
[42] H. Dai, H. Luo, J.F. Doyle, Dynamic pitching of an elastic rectangular wing in hovering motion, J. Fluid Mech. 693 (2011) 473–499.
[43] J. Young, S.M. Walker, R.J. Bomphrey, G.K. Taylor, A.L.R. Thomas, Details of Insect Wing Design and Deformation Enhance Aerodynamic Function and Flight Efficiency, Science 325 (2009) 1549–1552.
[44] J.H. Seo, T.L. Hedrick, R. Mittal, Mechanism and scaling of wing tone generation in mosquitoes, Bioinspir. Biomim. 15 (1) (2019) 016008.